FULL PAPER

An automated approach to fully self-gated free-running cardiac and respiratory motion-resolved 5D whole-heart MRI

Lorenzo Di Sopra[1] (iD) | **Davide Piccini[1,2]** (iD) | **Simone Coppo[1]** | **Matthias Stuber[1,3]** (iD) | **Jérôme Yerly[1,3]** (iD)

[1]Department of Diagnostic and Interventional Radiology, Lausanne University Hospital, Lausanne, Switzerland

[2]Advanced Clinical Imaging Technology, Siemens Healthcare, Lausanne, Switzerland

[3]Center for Biomedical Imaging, Lausanne, Switzerland

Correspondence
Jérôme Yerly, Lausanne University Hospital, Rue de Bugnon 46, BH-8-84, 1011 Lausanne, Switzerland.
Email: yerlyj.mri@gmail.com

Purpose: To develop a previously reported, electrocardiogram (ECG)-gated, motion-resolved 5D compressed sensing whole-heart sparse MRI methodology into an automated, optimized, and fully self-gated free-running framework in which external gating or triggering devices are no longer needed.

Methods: Cardiac and respiratory self-gating signals were extracted from raw image data acquired in 12 healthy adult volunteers with a non-ECG-triggered 3D radial golden-angle 1.5 T balanced SSFP sequence. To extract cardiac self-gating signals, central k-space coefficient signal analysis (k_0 modulation), as well as independent and principal component analyses were performed on selected k-space profiles. The procedure yielding triggers with the smallest deviation from those of the reference ECG was selected for the automated protocol. Thus, optimized cardiac and respiratory self-gating signals were used for binning in a compressed sensing reconstruction pipeline. Coronary vessel length and sharpness of the resultant 5D images were compared with image reconstructions obtained with ECG-gating.

Results: Principal component analysis–derived cardiac self-gating triggers yielded a smaller deviation (17.4 ± 6.1 ms) from the reference ECG counterparts than k_0 modulation (26 ± 7.5 ms) or independent component analysis (19.8 ± 5.2 ms). Cardiac and respiratory motion-resolved 5D images were successfully reconstructed with the automated and fully self-gated approach. No significant difference was found for coronary vessel length and sharpness between images reconstructed with the fully self-gated and the ECG-gated approach (all $P \geq .06$).

Conclusion: Motion-resolved 5D compressed sensing whole-heart sparse MRI has successfully been developed into an automated, optimized, and fully self-gated free-running framework in which external gating, triggering devices, or navigators are no longer mandatory. The resultant coronary MRA image quality was equivalent to that obtained with conventional ECG-gating.

KEYWORDS
3D radial trajectory, 5D whole-heart MRI, compressed sensing, coronary MRA, free-running, self-gating

1 | INTRODUCTION

In current clinical settings, cardiac MRI often suffers from both a limited ease-of-use and time inefficiency, which may hinder a more widespread use of cardiac MRI outside of dedicated academic centers with well-trained and highly specialized personnel. In recent years, a wide range of solutions have been proposed to simplify the workflow. As an alternative to conventional series of double oblique 2D images acquired over multiple breath-holds,[1-3] 3D cardiac MRI simplifies scan planning while also improving SNR and spatial coverage.[4,5] However, the longer acquisition time associated with 3D imaging often mandates a trade-off among spatial resolution, temporal resolution, and volumetric coverage. It also requires reliable cardiac and respiratory-motion compensation strategies to minimize motion artifacts. Adverse effects from cardiac motion are commonly avoided using electrocardiogram (ECG) triggering to synchronize the image acquisition with the cardiac cycle,[6,7] while respiratory motion is often suppressed using navigator-gated acquisitions.[8,9] However, the use of ECG-related lead placement, navigators, and planning affects workflow, ease of use, and setup time.

Recent developments of 4D cardiac motion-resolved MRI techniques have further simplified the workflow by removing the need for trigger delay adjustments and permitting reconstruction of time-resolved 3D volumes covering the entire cardiac cycle.[10,11] However, for such techniques, respiratory motion suppression remains a challenge and was addressed with either "gating,"[12,13] retrospective correction,[10,14] or image registration by combining or co-registering images at different respiratory positions.[11,15-17] Instead of discarding or co-registering data, a more recent approach aimed at resolving the different respiratory motion states, with a method called extra-dimensional golden-angle radial sparse parallel MRI,[18] which also has been applied to respiratory-resolved ECG-triggered coronary MRA.[19] This novel approach that exploits compressed sensing (CS) for the reconstruction of highly undersampled multidimensional data sets enables the reconstruction of 5D (x-y-z-cardiac-respiratory) images, in which data are sorted into both cardiac and respiratory motion-resolved states.[20] Although this concept still relied on the ECG that is recorded during the scan for cardiac gating purposes, the ECG signal is not always reliable, and rapid gradient switching and the magnetohydrodynamic effect that is amplified at higher magnetic field strength may lead to erroneous trigger signals.[21] For these reasons, alternative cardiac synchronization methods have been developed to reconstruct cardiac cine images without the need of an ECG signal.[11,22,23] These self-gating (SG) approaches have the potential to considerably simplify the workflow of cardiac MRI. Nevertheless, a fully SG approach in which cardiac *and* respiratory signals are directly extracted from the imaging data to leverage CS reconstruction has never been reported to our knowledge.

Here, we built on the ECG-gated 5D whole-heart MRI approach based on CS and respiratory self-navigation,[20] and developed the technique into an automated and optimized free-running framework for fully SG cardiac and respiratory motion-resolved noncontrast 5D imaging of the whole heart.

2 | METHODS

2.1 | Fully self-gated 5D whole-heart MRI framework

The study was performed in 12 healthy adult volunteers (age = 29 ± 5 years, 7 male) at the Lausanne University Hospital on a whole-body 1.5T clinical MR scanner (MAGNETOM Aera, Siemens Healthcare, Erlangen, Germany) with an 18-channel chest coil array and a 32-channel spine coil array for signal reception. The study was approved by the institutional review board and written, informed consent was obtained from all participants prior to MR scanning. The framework incorporated a previously reported prototype free-running 3D golden-angle radial balanced SSFP (bSSFP) sequence.[10] The prototype sequence continuously acquired data over a large number of cardiac cycles, while the acquisitions were segmented into multiple interleaves using the spiral *phyllotaxis* trajectory.[24] Each interleaf was rotated by the golden angle and was preceded by a readout oriented along the superior–inferior (SI) direction for cardiac and respiratory self-gating.[14] The following sequence parameters were used: TR/TE = 3.1/1.56 ms, 90° RF excitation angle, receiver bandwidth = 898 Hz/px, FOV = $220 \times 220 \times 220$ mm^3, 192 samples per readout, isotropic spatial resolution = $1.15 \times 1.15 \times 1.15$ mm^3, number of interleaves = 5749, number of lines per interleaf = 22, for a total of 126 478 radial lines and a constant total scan time of 14 minutes and 17 seconds. The acquisition used a non-slice-selective RF pulse, and each interleaf was preceded by a chemically shift-selective fat saturation pulse and 10 linearly increasing ramp-up RF excitations. The ECG signal was recorded with a standard 4-lead vector ECG device. The SG cardiac triggers were extracted from the SI readouts and compared with the reference standard ECG triggers to define the optimal approach. Thus, the selected SG signal was then used to sort the data into *cardiac* phases. Similarly, a *respiratory* motion signal was also extracted from the SI readouts using a previously described method[11,20] and used to partition the acquired data set into different respiratory states.[19] The 5D (x-y-z-cardiac-respiratory dimensions) motion-resolved data were then reconstructed with CS.[25] An overview of the study design is illustrated in Figure 1. The following sections describe the different automated components of the proposed SG approach.
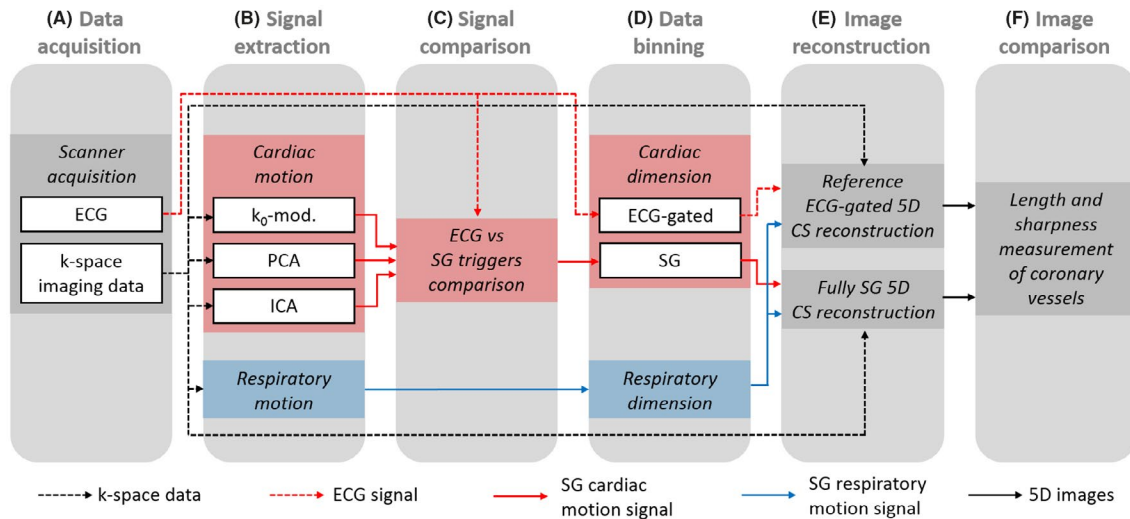
FIGURE 1 Schematic illustration of the study design. A, K-space imaging data and the electrocardiogram (ECG) signal were recorded during the MR acquisition. B, Self-gating (SG) cardiac and respiratory motion signals were extracted from the imaging data. Three different strategies (k_0 modulation, principal component analysis [PCA] on superior–inferior [SI] projections, and independent component analysis [ICA] on SI projections) were investigated for the extraction of the SG cardiac signals. C, Self-gating cardiac triggers were compared with the reference ECG triggers to determine the most precise strategy. D, K-space data were then sorted into cardiac and respiratory motion-resolved bins using the SG respiratory signal together with either the ECG or the best SG cardiac signal. E, These undersampled 5D motion-resolved data sets were then reconstructed using a compressed sensing (CS) framework. Each data set was reconstructed twice, first using the ECG-gated binning, then using the fully SG approach. F, Finally, images were compared by measuring the coronary vessel length and sharpness. In particular, the right coronary artery (RCA), left main coronary artery (LM), and left anterior descending artery (LAD) were investigated in both systole and middiastole

2.2 | Trajectory-dependent frequency component filtering

The segmented radial acquisition scheme used in this study supports the repeated and frequent sampling of SI readouts. The signal amplitudes of these readouts are modulated by the physiological motion that occurs over time. Furthermore, radial sampling is susceptible to trajectory imperfections caused by gradient timing delays,[26] eddy currents, and other sources. These trajectory imperfections not only affect image quality but also the extracted motion signals by adding an unwanted and trajectory dependent modulation to the physiological signals. The frequencies of this artifactual signal modulation are unfortunately in the same range as those of the physiological signals, hence interfering with the physiological signal extraction. However, as the frequency of this fluctuation is dependent on the golden-angle trajectory, it can still be separated from the physiological information and removed. For this purpose, a previously described approach[27] was adapted and applied to the extracted SG signals to filter out the trajectory-dependent modulations. These signals, initially available in the time domain (Figure 2A), were re-ordered as a function of the golden-angle k-space acquisition scheme (Figure 2B): SI projections were sorted with respect to the azimuthal angle of their corresponding interleaf. Because the physiological modulation is incoherent with the reordered data, a Butterworth IIR high-pass filter removed only the

slowly varying angle-dependent modulation (Figure 2D). Filter parameters (stopband = 0.0001 rad^{-1}, passband = 0.04 rad^{-1}) were manually selected by analyzing the frequency spectrum of the re-ordered signal, while the filter order was then automatically adjusted to ensure steep transitions between the passband and the stopband frequencies. Filtered (cleaned) data were then sorted back into their original temporal order (Figure 2C).

2.3 | Cardiac motion signal extraction

Three different strategies were implemented and investigated for their adequacy to extract cardiac motion signals from the SI readouts of noncontrast 3D radial free-running bSSFP imaging sequence: (1) analysis of the magnitude of the central coefficient of each SI readout (k_0) modulation,[22] (2) principal component analysis (PCA) of the SI projections,[11,20] and (3) independent component analysis (ICA) of the SI projections. The 3 pipelines are schematically illustrated in Figure 3.

For the k_0 modulation approach, the magnitude of the complex k-space central coefficient of all N_C coils (i.e., echo peak) was used. The temporal evolution of the echo peak is modulated by physiological motion and trajectory imperfections. To remove the effects of the latter, the previously described trajectory-dependent frequency component filtering was performed on each one of the N_C signals independently. The power spectral densities (PSDs) of these *cleaned* k_0 signals from all coils were then computed and analyzed

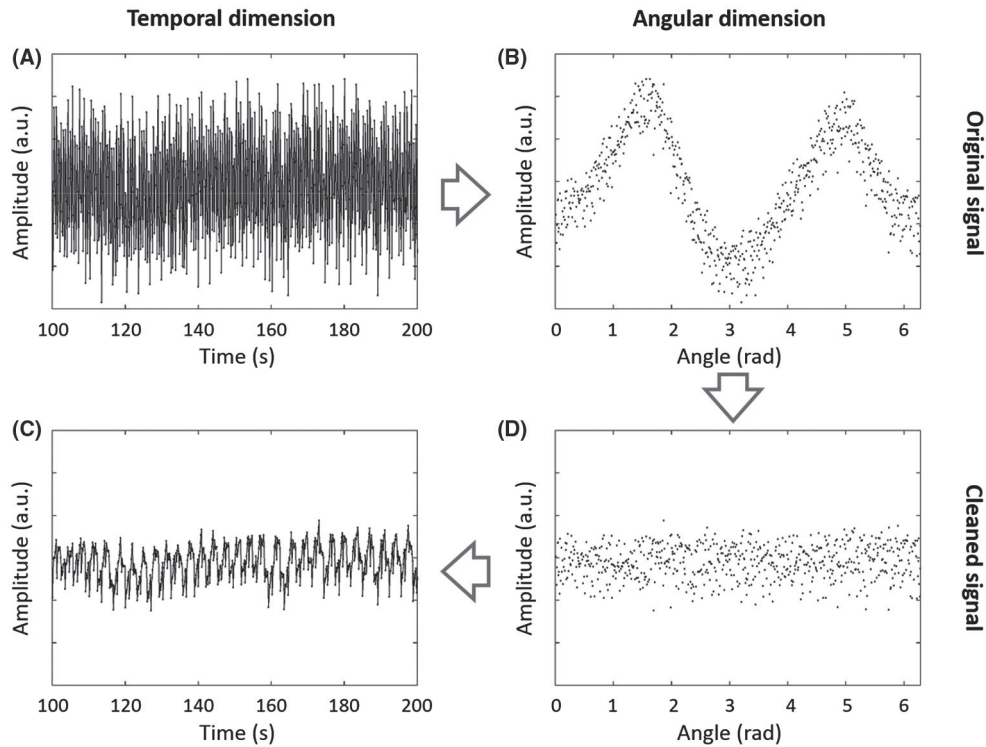**Temporal dimension**   **Angular dimension**

FIGURE 2   Example of a k_0 modulation signal that undergoes the trajectory-dependent frequency component filtering. The whole procedure is based on the concept of sorting SG signals according to a different ordering (angular rather than temporal), in which trajectory-dependent components are coherent while physiological information is incoherent, thus allowing for their differentiation and separation. A,C (left), The k_0 modulated signal in function of time over an interval of 100 seconds. B,D (right), The same signal reordered according to the interleaf azimuthal angle between 0 and 2π radians. A,B (top), The original signal before the trajectory-dependent frequency component filtering. C,D (bottom), The filtered (cleaned) signal. In (B), the angular dependency is characterized by a strong oscillation of the baseline signal as a function of the azimuthal angle. The oscillation is effectively removed in (D) through high-pass filtering. A comparison between (A) and (C) shows that, after removing the trajectory-dependent information, the signal variability is reduced and a periodic oscillation (consistent with respiratory motion) is now unveiled

to obtain the cardiac motion signal. To this end, a subject-dependent range of frequencies was automatically estimated for each subject to individually isolate the cardiac motion components. Hereby, the goal was to ignore the undesired frequencies not related to cardiac motion by adapting the filter bandwidth to the subject's specific PSD. The procedure is illustrated in Supporting Information Figure S1. Starting with frequencies between 0.5 Hz and 2.0 Hz, the algorithm automatically computed the PSD's center of mass within that interval. The boundary frequencies of the range were then refined by finding the minima of the valleys at lower ($F_{inf,c}$) and higher ($F_{sup,c}$) frequencies with respect to the center of mass ($F_{0,c}$). Among the N_C signals considered, the one yielding the highest energy in the defined range was selected as cardiac signal, Fourier-transformed back in the time domain, and further used for data sorting.

The second method for cardiac motion signal extraction was based on the PCA performed on SI projections.[11] Such navigator projections were obtained by computing the one-dimensional fast Fourier transform of the SI readouts for all coils. The magnitude of all SI projections was concatenated in a ($N_P \times N_C$)-by-N_S matrix, where N_P is the number of

samples acquired along each SI readout, and N_S is the number of acquired SI readouts during the scan. For this method, the trajectory-dependent frequency component filtering described previously was performed independently on each of the ($N_P \times N_C$) lines of the concatenated matrix. The PCA was then computed on the cleaned matrix along the ($N_P \times N_C$) direction. The PSDs of the first 10 principal components were subsequently computed and analyzed. The automatic subject-dependent frequency range selection, previously described for the first method, was applied to the first 10 principal components to determine the one that best described the cardiac motion information. The selected component was then transformed back in the time domain for further data sorting.

Similar to the PCA approach, the third method for cardiac motion signal extraction included an ICA on the concatenated SI projections after the trajectory-dependent frequency component filtering on the ($N_P \times N_C$)-by-N_S matrix. Consistent with the first 2 methods, PSDs of the independent components were computed, and the subject-dependent frequency range selection was used to automatically select the cardiac signal, to finally transform it back in the time domain.
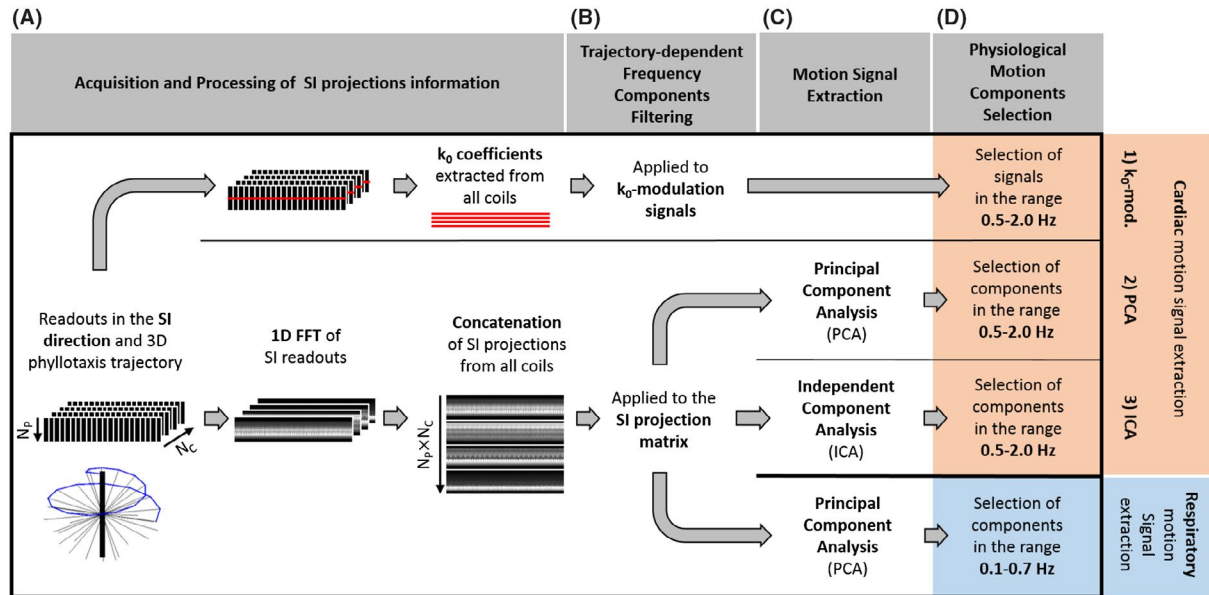
FIGURE 3 The main steps for cardiac and respiratory motion signal extraction, displayed in sequential order from left to right. A, Acquisition and preprocessing of the SI readouts. One interleaf of the 3D spiral phyllotaxis trajectory is displayed at the bottom-left corner with the SI readout shown as a solid thick black line. For the k_0 modulation approach (upper panel), the cardiac motion signal was extracted from the central k-space coefficients collected from all coils. For all of the other approaches (lower panel), the SI readouts were first 1-dimensional fast Fourier-transformed (FFT) and concatenated in a 2D matrix of SI projections also obtained from all coils. B, Trajectory-dependent frequency components filtering was either applied to the N_C k-space central coefficient modulation signals (upper panel) or to the $N_P \times N_C$ image-space signals of the 2D matrix of concatenated SI projections (lower panel). C, Principal component analysis (PCA) and independent component analysis (ICA) were performed on the SI projection matrix (lower panel) for motion signal extraction. In (D), cardiac and respiratory motion signals were specifically and automatically selected from the previously extracted motion signals based on their frequency components. For the cardiac motion signal, the automatic procedure searched for the signal with the highest energy in the frequency range 0.5-2 Hz. Similarly, the signal with the highest energy in the frequency range 0.1-0.7 Hz was selected as the respiratory motion signal

2.4 | Self-gated cardiac triggers extraction

After the cleaned cardiac signals from the 3 different approaches were available, trigger time points were extracted from the zero-crossings of these signals. To this end, signals were first interpolated using the Whittaker-Shannon (sinc) formula to increase the signal's temporal resolution 20-fold, allowing for a finer detection of cardiac triggers. A 2-step detection algorithm was implemented to be robust against eventual high-frequency oscillations that might corrupt the trigger estimation by introducing additional spurious zero-crossing locations. The steps correspond to 2 parallel and independent filtering procedures of the cardiac signal. As a first step, the cleaned cardiac signals were filtered with a narrow band-pass Butterworth filter to determine provisional peaks that roughly estimate the cardiac cycles. The stopband and passband frequencies of the band-pass filter were determined as described in cardiac motion signal extraction: $stopband_1 = F_{inf,c} - 0.2$ Hz; $passband_1 = F_{inf,c}$; $passband_2 = F_{sup,c}$; $stopband_2 = F_{sup,c} + 0.2$ Hz. As a second step, the original cleaned cardiac signals were filtered with a high-pass Butterworth filter ($stopband = F_{inf,c} - 0.2$ Hz; $passband = F_{inf,c}$), to remove only the signal offset and

baseline drift (Supporting Information Figure S1). These high-pass filtered signals were then used to detect zero-crossing locations right before (ascending) and right after (descending) the peaks previously found from the band-pass filtered signals. If multiple zero-crossing locations were found for the same cardiac cycle, the one associated with the steepest slope was chosen. Finally, the average slopes of the ascending and descending zero-crossing locations were computed, and those yielding the steepest average slope were used as SG cardiac triggers. An example of the trigger extraction procedure is illustrated in Figure 4.

2.5 | Cardiac trigger comparison: ECG-gated versus self-gated

Before addressing the comparison between the SG triggers (S) with the reference ECG triggers (R), potential shortcomings of the reference standard ECG signal have to be considered. Due to rapid gradient switching and the magneto hydrodynamic effect, R-waves are not always correctly detected,[21] thus leading to missed or false ECG triggers. In our study, the interval duration between consecutive ECG triggers as provided by the scanner hardware and software was measured to estimate
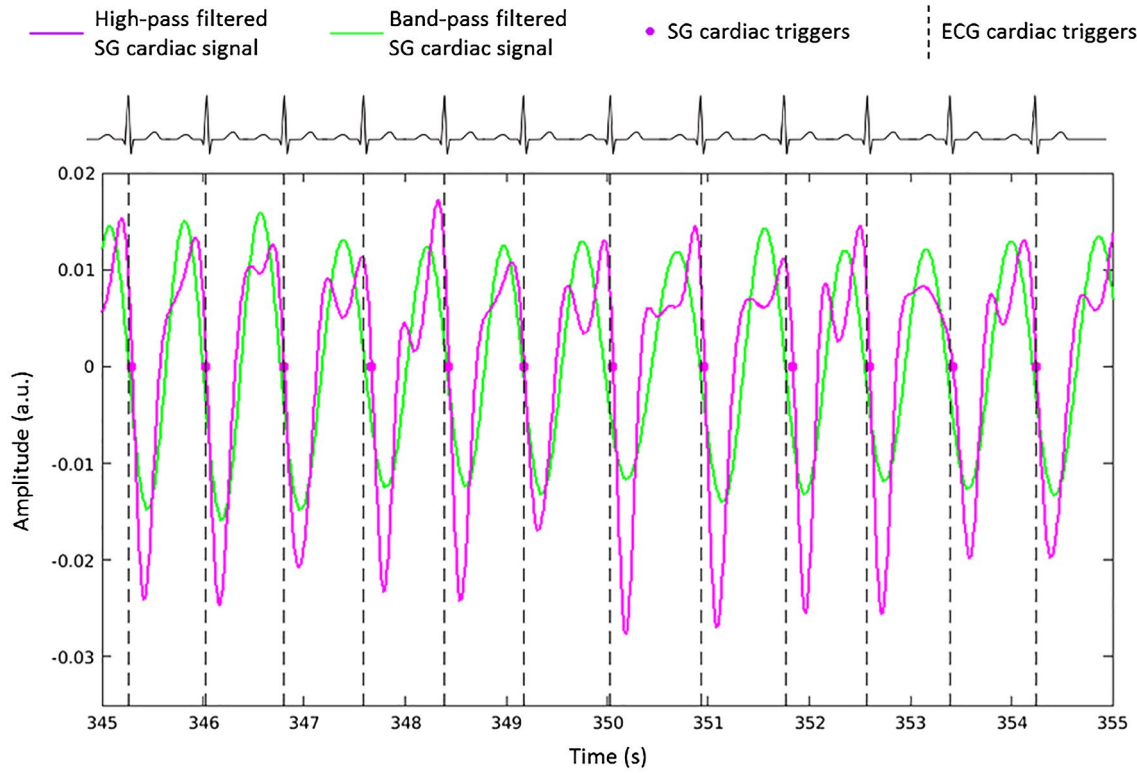
FIGURE 4 Example of the trigger extraction procedure from an estimated SG cardiac signal. The solid purple line (high-pass filtered SG cardiac signal) represents the SG signal after trajectory-dependent frequency component filtering, whereas the solid green line (band-pass filtered SG cardiac signal) refers to the band-pass filtered version of the same signal. The 2 signals are used in the 2-step algorithm for SG cardiac triggers estimation. The purple dots represent the estimated SG cardiac triggers, detected at the zero-crossing of the high-pass filtered SG cardiac signal. In this case, the descending points were found to have the steepest average slope. As a reference, the time-matched ECG cardiac triggers are displayed as vertical dashed lines to allow visual comparison with the SG triggers

the percentage of missed triggers. An interval duration greater than $1.5M$ or less than $0.5M$ (where M is the moving median estimated over 20 consecutive intervals) was considered to be erroneous and was then excluded from the comparison with the corresponding SG interval. For the following analysis, the acquired data sets were separated into 2 groups: the first group (group 1) included data sets with 1% or less of identified erroneous ECG triggers, whereas the second group (group 2) consisted of the remainder of the data sets, in which at least 1% of the RR intervals was found outside of this range. For comparison purposes, the percentage of missed SG triggers was also estimated following the same procedure.

To statistically evaluate the SG cardiac triggers obtained with the 3 methods described previously, the intervals between consecutive R-peaks of the ECG signal, $R_{n+1} - R_n$, were measured and compared with the intervals between triggers extracted from the SG signals, $S_{n+1} - S_n$. As a measure of precision, the SD σ between ECG R-peak intervals and SG trigger intervals was calculated as

$$\sigma = \sqrt{\frac{1}{N-2} \sum_{n=1}^{N-1} \left\{ \left[\left(S_{n+1} - S_n \right) - \left(R_{n+1} - R_n \right) \right] - \mu \right\}^2}, \quad (1)$$

where the average difference μ between cardiac intervals measured with ECG and SG signals over N heartbeats is given by

$$\mu = \frac{1}{N-1} \sum_{n=1}^{N-1} \left[\left(S_{n+1} - S_n \right) - \left(R_{n+1} - R_n \right) \right] \quad (2)$$

A smaller SD indicates a better precision between the duration of cardiac intervals measured with ECG and SG signals. The SG method that produced the smallest SD relative to the ECG intervals was then implemented as part of the fully automated SG pipeline. The mean SD $\hat{\sigma}$ was estimated over all data sets as well as separately for group 1 ($\hat{\sigma}_{G1}$) and group 2 ($\hat{\sigma}_{G2}$). A Student's paired t-test with 2-tailed distribution was used to compare the 2 groups.

2.6 | Respiratory motion signal extraction

The extraction of the respiratory motion signal was adapted from a previously reported and validated technique that is based on the PCA of SI projections.[11] However, and as described for the cardiac signal extraction previously, the matrix of combined SI projections was also cleaned by the

trajectory-dependent frequency component filtering before extracting the respiratory signal. Similarly, the selection of the best principal component to describe the respiratory motion was borrowed from the cardiac motion signal extraction pipeline, with the initial frequency range set to 0.1-0.7 Hz and then automatically adjusted to the subject-specific PSD (Supporting Information Figure S1). This pipeline is also visualized in the schematic of Figure 3.

2.7 | Data sorting

The SG cardiac and respiratory motion signals were used to sort the continuously acquired 3D radial readouts into a 5D motion-resolved (k_x-k_y-k_z-cardiac-respiratory) data set. The amplitude of the SG respiratory motion signal was used to partition the data into 4 respiratory motion states ranging from end-inspiration to end-expiration. The division of the partitions was automatically determined to yield the same amount of data in each partition. Next, the SG cardiac triggers were used to sort the acquired data into cardiac phases of 50-ms duration each and without view sharing between consecutive partitions. For comparison, a reference ECG-gated 5D motion-resolved data set was also reconstructed using the ECG triggers instead of the SG triggers for cardiac binning. In the case in which missed or false ECG triggers were detected (see section 2.5), a correction algorithm was applied to estimate the time of the corrupted triggers so that no imaging data were discarded from the reconstruction. The algorithm estimated the missed ECG trigger times by averaging the RR-interval duration of 4 neighboring triggers. This ECG-based binning approach corresponds to a previously reported strategy for 5D imaging.[20] Data sets binned with the 2 different approaches, hereafter referred to as ECG-gated and fully SG, were then reconstructed with the same exact algorithm.

2.8 | Five-dimensional image reconstruction

The reconstruction of 5D whole-heart images from highly undersampled data sets was performed using a k-t sparse SENSE algorithm,[18,20] which exploited sparsity along both the cardiac and respiratory dimensions. The reconstruction was performed twice for each data set: first using the SG triggers to resolve for cardiac motion, then using the reference ECG triggers with the same purpose. Respiratory motion resolution was the same for both reconstructions. The reconstruction was performed by solving the following optimization problem:

$$\mathbf{m} = \arg\min_{\mathbf{m}} \|\mathbf{FCm} - \mathbf{s}\|_2^2 + \lambda_r \|\nabla_r \mathbf{m}\|_1 + \lambda_c \|\nabla_c \mathbf{m}\|_1 \quad (3)$$

where $\mathbf{m}$ is the resultant 5D reconstructed image; $\mathbf{F}$ is the nonuniform fast Fourier transform operator; $\mathbf{C}$ refers to the coil sensitivities; $\mathbf{s}$ refers to the acquired k-space data set; ∇_r and ∇_c are the first-order difference operators along the cardiac and respiratory dimensions, respectively; and λ_r and λ_c represent the corresponding regularization weights, which were experimentally optimized to be a tradeoff between residual aliasing and compression artifacts, and were set to be constant with $\lambda_c = 0.005$ and $\lambda_r = 0.05$ for all reconstructions. The optimization problem was solved using the nonlinear conjugate gradient with backtracking linesearch.

2.9 | Image analysis: quantitative assessment and statistical analysis

For both ECG-gated and fully SG 5D data sets, 1 systolic cardiac phase (maximal contraction of the left ventricle) and 1 middiastolic cardiac phase (quiescent period of the left ventricle) were selected at end-expiration. These static motion-resolved 3D images were then processed using SoapBubble[28] to compute the vessel length and vessel sharpness of the right coronary artery (RCA), left main coronary artery (LM), and left anterior descending artery (LAD) on the reformatted images. For the sharpness, only the first 4 cm of the proximal sections of the coronary arteries were included. These measurements were performed by an unblinded reader (R_{1A}). RCA vessel length and sharpness during middiastole were then measured again by 2 blinded readers (R_{1B} and R_2), where R_{1B} is the same reader as R_{1A}, yet blinded, and the time between the first and the second analysis was 1 year. A Student's paired t-test with 2-tailed distribution and linear regression were used to compare the vessel length and sharpness of the coronary arteries obtained with the ECG-gated and the fully SG approach, as well as to compare the intra-observer and interobserver variability in the blinded evaluation of the RCA. A p-value less than .05 was considered statistically significant.

3 | RESULTS

The extraction of SG physiological motion signals succeeded in all cases, and the whole pipeline, completed by data binning and CS reconstruction of 5D motion-resolved data sets, worked fully automatically with no exceptions. The trajectory-dependent frequency component filtering of the SG signals effectively removed artifactual frequency components introduced by the trajectory during the acquisition and enabled automated and robust estimations of cardiac and respiratory motion signals (Figure 5).

The percentage of missed ECG triggers across all subjects was $6.9 \pm 8.6\%$ (Table 1). Considering the 1% threshold applied to the fraction of missed ECG triggers, the 12 subjects were equally divided into 2 groups. Group 1 (subjects 1, 7-11) showed an average missed ECG triggers fraction of $0.1 \pm 0.1\%$, whereas group 2 (subjects 2-6, 12)
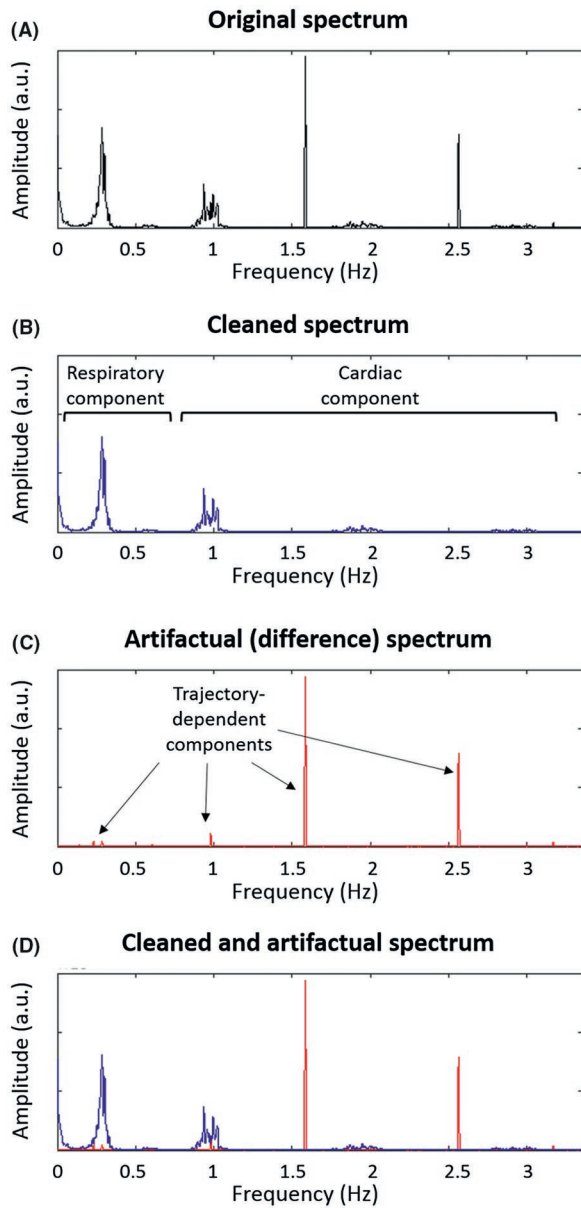
FIGURE 5 Spectra comparison between k_0 modulation signals before and after the trajectory-dependent frequency component filtering. A, The original spectrum shows an example of PSD computed on a k_0 modulation signal extracted from SI readouts. Frequency components of cardiac and respiratory physiological motion are clearly visible, together with sharp frequency components introduced by trajectory dependency. B, The cleaned spectrum shows the PSD from the same signal after application of the trajectory-dependent frequency component filtering. Trajectory-dependent components are now suppressed, whereas the physiological information remains intact. C, The artifactual spectrum shows the difference between (A) and (B). Only the trajectory-dependent information is left, revealing some components previously submerged by superimposed physiological motion frequencies. D, The cleaned and artifactual spectrum shows the superposition of (B) and (C), which highlights that physiological and artifactual components can overlap (i.e., they can be located on the same frequencies)

showed a significantly larger fraction of missed ECG triggers: $13.6 \pm 7.2\%$, with a *p*-value of 0.02. These 2 groups were considered for the rest of the analysis. The percentage of missed SG triggers was 0% across all subjects and for all SG methods (Figure 6).

The precision of the estimated SG cardiac triggers, relative to their ECG-derived counterparts, is summarized in Table 1 for all 3 investigated methods. Looking at the difference in RR duration measured using the ECG and SG signal extraction, the SD $\hat{\sigma}$ across all subjects amounts to 45.5 ± 27.7 ms for the k_0 modulation method, 28.2 ± 15.3 ms for PCA, and 29.0 ± 17.7 ms for ICA. When considering group 1 and group 2 separately (i.e., less than 1% versus more than 1% of missed ECG triggers), the SD of each group was $\hat{\sigma}_{G1} = 26.8 \pm 7.5$ ms versus $\hat{\sigma}_{G2} = 65 \pm 26.8$ ms for k_0 modulation, $\hat{\sigma}_{G1} = 17.4 \pm 6.1$ ms versus $\hat{\sigma}_{G2} = 39 \pm 14$ ms for PCA, and $\hat{\sigma}_{G1} = 19.8 \pm 5.2$ ms versus $\hat{\sigma}_{G2} = 38.2 \pm 21.5$ ms for ICA. The difference between group 1 and group 2 was statistically significant for the k_0 modulation and PCA methods ($P_{k0} = .035$, $P_{PCA} = .034$), and almost significant for the ICA method ($P_{ICA} = .061$). Based on these results,

TABLE 1 Results summarizing the precision of the SG cardiac triggers estimated using the 3 methods investigated in this study (k_0 modulation, PCA on SI projections, and ICA on SI projections)

Subject	Missed ECG triggers (Group)[a]	ECG vs SG trigger precision (ms)		
		k_0 modulation	PCA	ICA
n.1	0.2%[(1)]	35.3	21.9	21.5
n.2	22.8%[(2)]	43.8	34.1	39.4
n.3	9.6%[(2)]	55.8	30.8	25.1
n.4	5.0%[(2)]	114.2	64.7	34
n.5	20.5%[(2)]	61.2	45.1	80.1
n.6	8.1%[(2)]	41.6	26.6	21.5
n.7	0.2%[(1)]	31.4	18.0	17.3
n.8	0.1%[(1)]	13.3	10.0	11.3
n.9	0.0%[(1)]	24.1	13.7	26.8
n.10	0.0%[(1)]	25.3	14.2	20.8
n.11	0.1%[(1)]	26.6	26.7	21
n.12	15.7[(2)]	73.5	32.8	29.3
All subjects	$6.9\% \pm 8.6\%$	45.5 ± 27.7	28.2 ± 15.3	29.0 ± 17.7
Group 1 ($\leq 1\%$)	$0.1\% \pm 0.1\%$	26.0 ± 7.5	17.4 ± 6.1	19.8 ± 5.2
Group 2 ($> 1\%$)	$13.6\% \pm 7.2\%$	65 ± 26.8	39 ± 14	38.2 ± 21.5

[a]The second column shows the estimated fraction of missed ECG triggers; indices within parentheses indicate the association to the first ($\leq 1\%$ of missed ECG triggers) or second ($> 1\%$ of missed ECG triggers) group. The averaged results for the 2 separate groups are reported separately in the 2 rows at the bottom of the table.
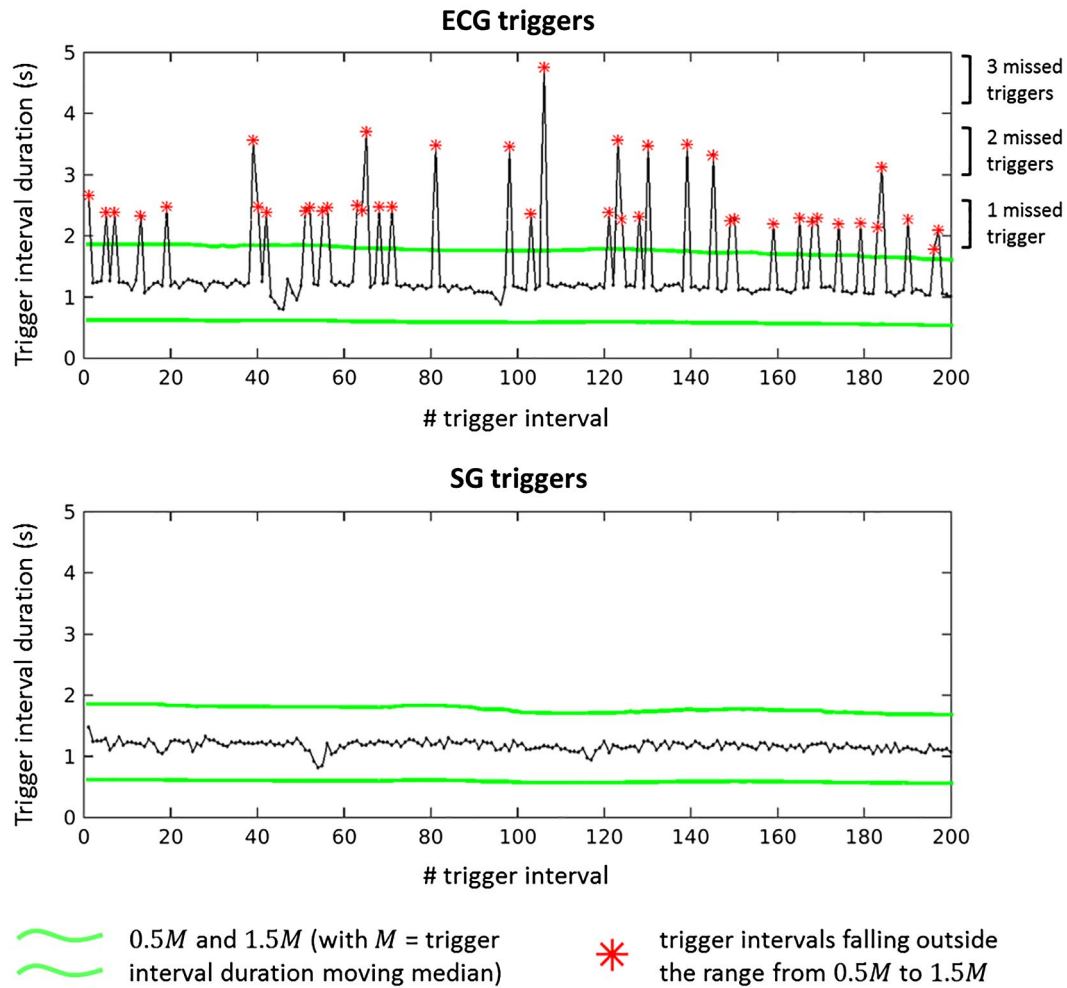
FIGURE 6 Interval durations between consecutive triggers from ECG information (top panel) and from SG signal (bottom panel) in the same data set are compared. The first 200 cardiac intervals of the acquisition are displayed. The green lines represent the $0.5M$ (lower line) and $1.5M$ (upper line) boundaries, where M is the moving median estimated on the interval duration signal (black dots). Trigger intervals with duration falling outside the region limited by the 2 boundaries are considered erroneous and are marked with a red asterisk. Red asterisks can be intuitively grouped according to the number of missed ECG triggers (N missing triggers): erroneous trigger intervals are approximately a multiple integer of the moving average cardiac cycle duration. No missed triggers are found in any of the SG cardiac signals, as shown in this example

the PCA was selected as the most precise method and was used for cardiac SG signal extraction moving forward. The vessel length and sharpness obtained with this SG signal are summarized in Table 2 for systole and diastole and compared with images generated using the ECG. The RCA, LM, and LAD were visible in all 12 subjects, in both systole and diastole, and for both ECG-gated and fully SG approaches. Vessel length and sharpness could always be measured, with the only exception of the LM + LAD in 3 subjects, in whom visualization was impaired with both ECG-gating and SG. None of the measured parameters showed a statistically significant difference between the ECG-gated and SG approaches (all $P > .06$). This statement holds true for both the left and right coronary arterial system and for both systole and middiastole. The blinded evaluation provided 3 results. First, for all readers (R_{1A}, R_{1B}, R_2) and both coronary length and sharpness, measures in the fully SG and ECG-gated images were never statistically different (all $P \geq .06$). Second, the intra-observer variability of the first reader (R_{1A} versus R_{1B}) provided no significant difference ($P \geq .11$). Third, the interobserver variability between the 2 blinded readers (R_{1B} versus R_2) provided an almost significant difference in the coronary length measurement ($P = .06$ and $P = .08$ for ECG-gated and SG images, respectively), but not for the vessel sharpness ($P \geq .54$ for both ECG-gated and SG images).

End-expiratory and end-inspiratory, as well as systolic and middiastolic multiplanar reformats, extracted from the fully SG 5D whole-heart images are shown in Figure 7, highlighting the differences in the respiratory position and in the contractile state of the heart. Animated images of the same data set along both cardiac and respiratory dimensions can be found in Supporting Information Videos S1 and S2. Images of RCA and left anterior descending vessels from 2 different

TABLE 2 Vessel length and sharpness for the RCA and LM + LAD

RCA

Length				Sharpness			
Systole		Middiastole		Systole		Middiastole	
ECG-gated	SG	ECG-gated	SG	ECG-gated	SG	ECG-gated	SG
8.4 ± 2.3 cm	8.4 ± 2.3 cm	7.8 ± 2.6 cm	8.3 ± 2.8 cm	44.9 ± 10.1%	46.3 ± 10.1%	41.9 ± 13.1%	40.5 ± 12.6%
$P = .88$		$P = .15$		$P = .45$		$P = .24$	
y = 0.92x + 0.59 cm		y = 1x + 0.47 cm		y = 0.81x + 9.8%		y = 0.92x + 1.9%	
$R^2 = 0.84$		$R^2 = 0.87$		$R^2 = 0.66$		$R^2 = 0.91$	

LM + LAD

Length				Sharpness			
Systole		Middiastole		Systole		Middiastole	
ECG-gated	SG	ECG-gated	SG	ECG-gated	SG	ECG-gated	SG
9.1 ± 4.3 cm	9.7 ± 4.1 cm	10.1 ± 4.1 cm	9.1 ± 4.1 cm	35.8 ± 6.9%	35.6 ± 8.5%	37.8 ± 10.8%	33.4 ± 9.7%
$P = .47$		$P = .06$		$P = .94$		$P = .08$	
y = 0.78x + 2.65 cm		y = 0.93x − 0.23 cm		y = 0.95x + 1.83%		y = 0.69x ± 7.48%	
$R^2 = 0.65$		$R^2 = 0.87$		$R^2 = 0.58$		$R^2 = 0.58$	

Note: The displayed results are the parameters' mean and SD estimated over the 12 subjects. Coronary length and sharpness showed no significant difference between the ECG-gated and the SG approach under any of the conditions evaluated (end-systolic and middiastolic phase of the cardiac cycle), as confirmed by the *p*-values that are always greater than .06. The linear regression and coefficient of determination also confirm a good agreement between the scores in the reference ECG-gated and the SG images. For this comparison, the best method for SG cardiac trigger estimation (PCA on SI projections) was considered.

subjects are shown in Figure 8, where corresponding multi-planar reformats from ECG-gated and fully SG CS reconstructions are compared.

4 | DISCUSSION

A fully automated SG approach to free-running 5D MR imaging of the heart at 1.5 T and without the need for contrast agents, navigators, external gating, or triggering devices has successfully been implemented and tested. This current framework offers the simultaneous and retrospective interrogation of anatomy and function and has several potential strengths. First, it improves ease of use by reducing operator dependency during clinical cardiac MRI workflow. The proposed SG approach no longer requires sophisticated planning, nor placement of navigator and ECG electrodes for triggering purposes, nor sequence timing relative to physiological motion (trigger delay and acquisition window width), which otherwise all have to be performed by a skilled operator. Second, and because data collection is performed in a free-running mode without synchronization to respiration and cardiac cycle, data collection is highly efficient, as time for planning, recovery periods in-between breath-holds, and trigger delays to image the heart during a period of relative quiescence are almost entirely removed. Finally, and owing

to the golden-angle radial acquisition scheme together with CS, the collected data can be reordered rather freely and the temporal position within the cardiac cycle, the width of the reconstruction window and even the respiratory level for which the data should be displayed, can be chosen flexibly after the scan. Clearly, the work presented here builds on the previous experience of Coppo et al,[10] who were among the first to demonstrate the feasibility of a noncontrast bSSFP free-running approach for 4D imaging of the heart on a 1.5 T system. In that particular study, coronary anatomy and left ventrical function were concomitantly acquired in 1 single uninterrupted scan, providing a meaningful step toward an automated and comprehensive framework for anatomical and functional imaging of the heart. However, this implementation still mandated an ECG for binning purposes, and simple, linear correction for respiratory motion was used. To this end, Pang et al[11] demonstrated 4D whole-heart imaging with a fully SG approach, in which cardiac and respiratory motion signals are directly and reliably extracted from the imaging data, and more sophisticated motion fields are exploited to account for respiratory displacement of the heart during reconstruction. In their implementation, data were acquired with a gradient echo sequence at 3 T, and an extracellular contrast agent was intravenously administered to enhance contrast between the blood pool and the myocardium. In our implementation, a bSSFP sequence at 1.5 T
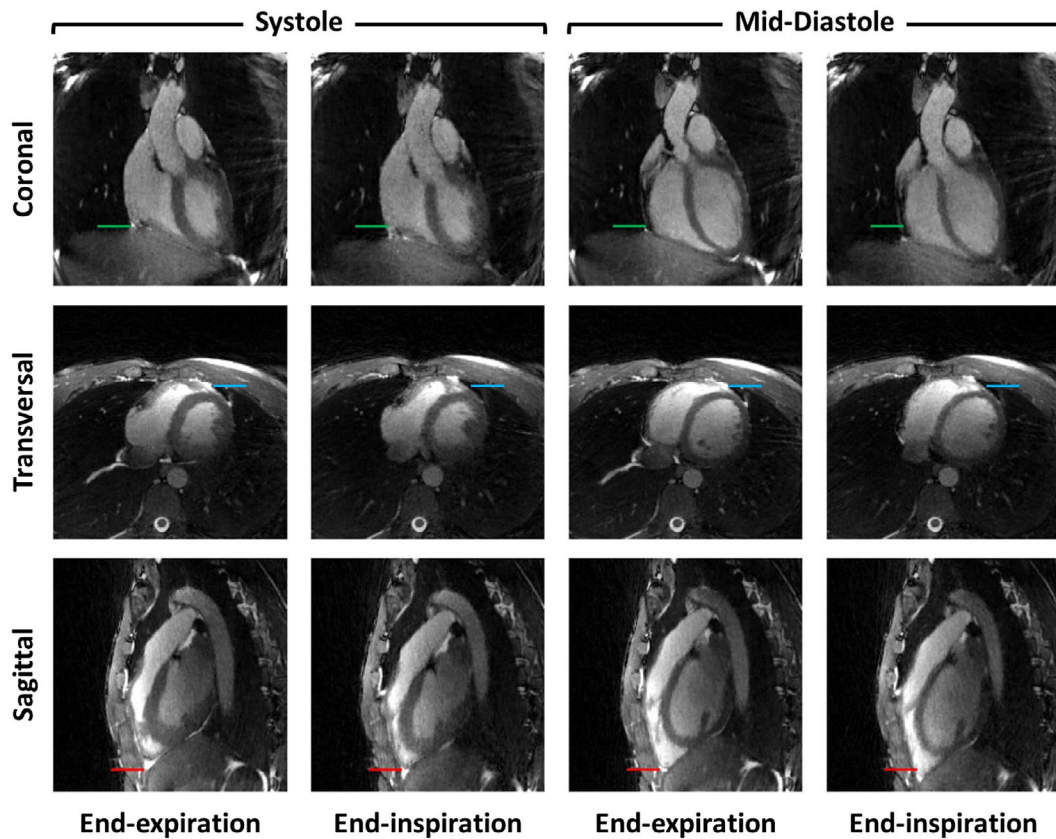
FIGURE 7 Coronal, transversal, and sagittal cross sections from the same data set, reconstructed with SG motion signal for both cardiac and respiratory dimensions. Two respiratory states (end-expiration and end-inspiration) and 2 cardiac phases (systolic and middiastolic) are displayed. The corresponding green, blue, and red lines in the 3 visualizations help visualize the displacement caused by respiration. The differences between the systolic and the middiastolic phases of the cardiac cycle can be visually appreciated in the size of the left ventricle blood pool and myocardium
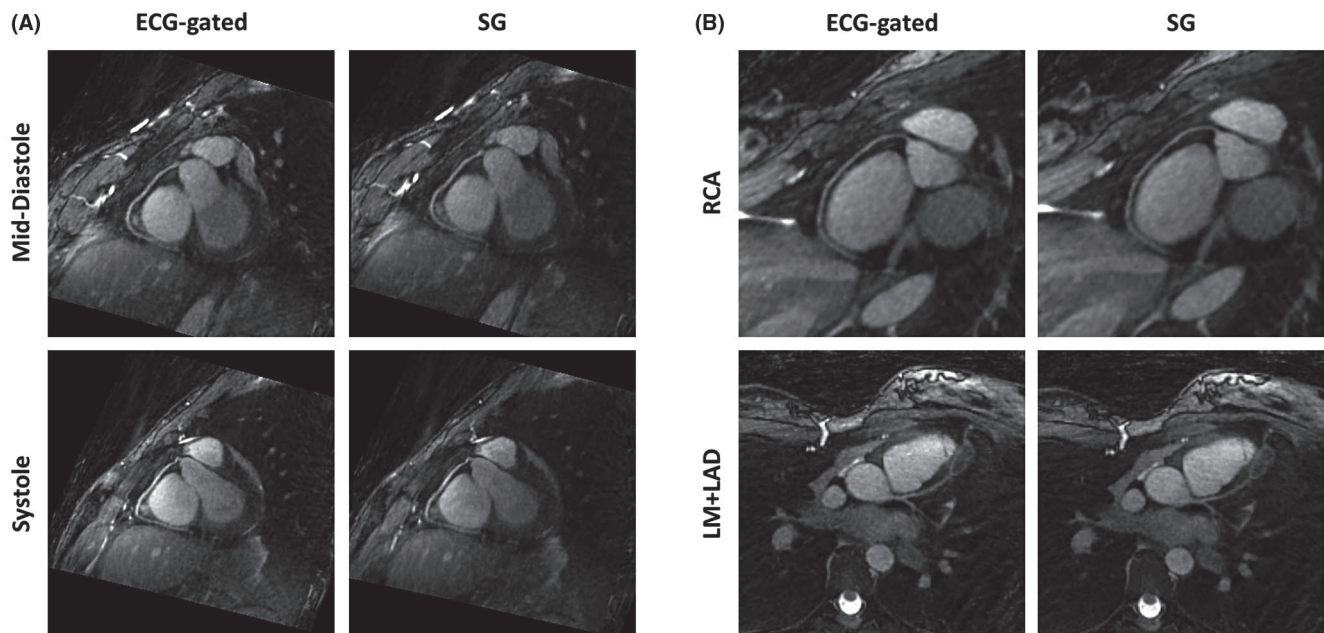

FIGURE 8 A, Reformatted images of the RCA obtained with the ECG-gated (left) and fully SG (right) approaches. Images are extracted from the middiastolic (upper) and systolic (lower) phases of the cardiac cycle and during end-expiration. B, Reformatted images of the right coronary artery (RCA) (upper) and left main coronary artery (LM) + left anterior descending artery (LAD) (lower) obtained with the ECG-gated (left) and fully SG (right) approaches. Images are extracted from middiastolic phases of the cardiac cycle and during end-expiration

provided enough contrast between the blood pool and the myocardium; therefore, injection of a contrast agent was not mandatory, although it remains an option. In addition, we used motion-resolved reconstruction using CS, and it is anticipated that the use of motion fields applied to different motion-resolved respiratory levels may also help further improve image quality. Work by Piccini et al[19] and Feng et al,[20] a clear starting and reference point of this study, showed that the introduction of CS reconstruction can provide additional dimensions to the reconstructed images, enabling 4D and even 5D whole-heart visualization with motion-resolved reconstruction of both cardiac and respiratory components. Although the ECG still had to be recorded for the cardiac motion–resolved reconstruction in these studies, the approach proposed here no longer mandates an ECG for motion-resolved reconstruction, and the cardiac signal can be extracted directly and reliably from the acquired imaging data. However, this study also showed that SG signal extraction from free-running golden-angle 3D radial bSSFP imaging at 1.5 T is not straightforward. Although only the SI readouts are considered for motion extraction, which are the same for every spiral interleaf, and, therefore, do not depend on their trajectory angle, trajectory-dependent and undesired frequency components are visible in the Fourier spectra of the cardiac and respiratory SG signals. These trajectory-dependent modulations result primarily from eddy currents that depend on gradient history and more specifically on the angle of the last readout before the SI acquisition.[29-31] Although such artifactual signals in a frequency range very similar to that of the physiological signals represents a critical challenge to the blind source separation problem, the proposed trajectory-dependent frequency component filtering clearly compensates for unwanted angular dependencies of the SG signal. With the proposed correction, separation of wanted and unwanted signal components became feasible, and the quality of the extracted signal critically enables automation of the procedure that provides precise trigger points. However, to what extent this may hold true for other types of trajectories, imaging sequences, or field strengths remains to be elucidated.

All 3 investigated methods for cardiac motion signal extraction proved to be effective in that they provided SG triggers that showed a good correlation with the ECG signal, which remains the mainstay of cardiac motion synchronization. Of note, the PCA method showed the highest precision among all 3 methods, which corroborates the findings about the good performance of this technique for cardiac and respiratory motion signal extraction of others.[11] In particular, Pang et al[11] reported an average SD value of the difference between ECG and SG trigger times of 30.9 ± 2.8ms at 3 T after contrast and using gradient echo. This is in line with the findings presented in this study, which yielded a very similar SD of 28.2 ± 15.3 ms.

The cardiac SG approaches afford fundamental advantages when compared with the commonly used ECG: The most important is that they are no longer affected by common sources of interference such as the magnetohydrodynamic effect or gradient switching, which may pose challenges for R-wave detection of the ECG. In our study conducted at 1.5 T, missed ECG triggers were observed in 50% of the healthy adult volunteers (group 2), in whom the amount of missed triggers ranged from 5% to more than 20% of the total number of heartbeats happening during the scan. In contrast, and according to our definition of missed triggers, none were found for any of the 3 investigated SG approaches. This can probably be attributed to the fact that the volume change of the heart is the primary source of the signal for SG, and contrary to the ECG, this signal is not adversely affected by blood flow in a magnetic field or gradient switching. Furthermore, as SG obviates the need for ECG lead placement or repositioning in the case of suboptimal R-wave detection, an improved overall ease-of-use and reduced operator dependency may be expected. Nevertheless, while SG worked well in all subjects of our study cohort, the behavior, robustness, and effectiveness of SG in patients and in the presence of arrhythmias remains to be investigated as a next step. Preliminary attempts of resolving arrhythmic cardiac cycles with different lengths in patients with atrial fibrillation have recently been investigated for 2D imaging.[32] The proposed SG framework lays the foundation to extend this concept to 3D imaging.

Still, some aspects of the SG techniques for cardiac motion estimation remain to be further discussed. First, the extraction of motion directly from the signal coming from the full field of view implies that not only cardiac but a superposition of several motion components is detected. However, and provided that cardiac and respiratory signals have little or no overlap in the frequency domain, these can rather easily be separated. As far as lower-frequency motion components, including patient bulk motion or respiratory drift are concerned, this has not been studied and remains to be further investigated. Another challenge pertains to hysteresis effects of the respiratory motion cycle,[33] which theoretically may lead to incorrect binning for CS reconstruction. Another aspect that deserves further investigation relates to the phase shift between the R-wave and the SG triggers. The motion information extracted from the imaging data is directly related to signal intensity variations, but the temporal relation between the ECG and the SG triggers is still not unequivocally defined. In practice, this only leads to a cyclic shift of the bins used for CS reconstruction. This effect is illustrated in Supporting Information Videos S1 and S2: to show the respiratory motion (middle row) and a static 3D volume (bottom row) from both the ECG-gated and SG reconstructed images, the same bin along the cardiac motion dimension was selected. However, because of this cyclic shift, the selected bin corresponds to different phases of the cardiac cycle, with systole and diastole shown in Supporting Information

Videos S1 (ECG-gated) and S2 (SG), respectively. However, this may not necessarily affect the visualization of anatomy or function. Nevertheless, future work should investigate whether particular features of the SG cardiac signal may even be matched to specific phases within the cardiac cycle, so that the binning procedure may reach another level of sophistication. Finally, a comparison of the obtained fully SG 5D data sets with reference ECG-triggered and navigator-gated cardiac images may help characterize the proposed approach. Nevertheless, a good agreement between ECG-gated 5D images and images obtained with ECG triggering and navigator gating has already been reported by Feng et al.[20] Provided the equivalence of image quality obtained here between ECG-gated and fully self-gated 5D imaging, such a comparison may only provide a limited amount of new information.

This study aimed at implementing a more efficient and practical approach to the whole-heart MRI framework that could challenge existing paradigms, which usually include synchronization of the data acquisition with the ECG, repeated breath-holds, or information derived from respiratory navigators. Indeed, free-running acquisitions[10,34-36] and SG approaches[23,37,38] may have the potential to redefine such paradigms, and to remove some of the main obstacles in contemporary cardiac MRI, not only by minimizing operator dependency and improving ease-of-use, but also by making selected elements of a cardiac MRI exam more time-efficient. Although fat saturation and ramp-up pulses still prevent us from further improving time efficiency of our imaging sequence,[10] implementing bSSFP with spectrally selective water RF excitation pulses such as those proposed in Bastiaansen and Stuber[39] may obviate the need for these periodic, short interruptions of the sequence and provide a further improved duty cycle. It may also be argued that the here-described fully SG method may help address several challenges in contemporary cardiac MRI. Scan planning is substantially facilitated, as 1 scout scan suffices to localize the heart in 3D, and operator involvement is further minimized provided that sequence-timing parameter modifications, plane orientations, navigator settings, and navigator localization no longer need to be adjusted. However, with the fully SG approach, the emphasis shifts from a rather complex and involved image-acquisition procedure as we know it today to how to best extract the relevant information after the fact, even though this comes at the price of a more computationally expensive image reconstruction. The timepoint for which images are reconstructed in the cardiac cycle, their temporal resolution, and at which respiratory level they should be extracted can freely and retrospectively be defined by the operator to best answer the clinical question at hand. However, this ultimately and inevitably leads to a large amount of data or a vast parameter space that needs to be interrogated: The extraction of information that best answers the question of the operator may ultimately be guided by machine learning.[40,41]

5 | CONCLUSIONS

A motion-resolved 5D CS whole-heart sparse MRI methodology was successfully developed into an automated and fully SG free-running framework, in which ECG triggering, gating, navigators, or contrast media are no longer needed. As compared with the reference standard ECG, PCA has been identified as the most precise method for SG cardiac motion signal extraction, but trajectory-dependent frequency component filtering was mandatory to remove artifacts from the SG signals and to enable automation. Applied to coronary MRA, fully SG 5D MRI led to image quality that is equivalent to that from 5D images reconstructed with the reference-standard ECG. This technique may help address some of the major hurdles in contemporary cardiac MRI that include operator involvement, operator dependency, and time inefficiency.

ORCID

Lorenzo Di Sopra https://orcid.org/0000-0003-3426-9457
Davide Piccini https://orcid.org/0000-0003-4663-3244
Matthias Stuber https://orcid.org/0000-0001-9843-2028
Jérôme Yerly https://orcid.org/0000-0003-4347-8613

REFERENCES

1. Bluemke DA, Boxerman JL, Atalar E, McVeigh ER. Segmented k-space cine breath-hold cardiovascular MR imaging. I: Principles and technique. *AJR Am J Roentgenol*. 1997;169:395–400.

2. Kramer CM, Barkhausen J, Flamm SD, Kim RJ, Nagel E; Society for Cardiovascular Magnetic Resonance Board of Trustees Task Force on Standardized Protocols. Standardized cardiovascular magnetic resonance (CMR) protocols 2013 update. *J Cardiovasc Magn Reson*. 2013;15:91.

3. Kilner PJ, Geva T, Kaemmerer H, Trindade PT, Schwitter J, Webb GD. Recommendations for cardiovascular magnetic resonance in adults with congenital heart disease from the respective working groups of the European Society of Cardiology. *Eur Heart J*. 2010;31:794–805.

4. Plein S, Ridgway JP, Jones TR, Bloomer TN, Sivananthan MU. Coronary artery disease: assessment with a comprehensive MR imaging protocol—initial results. *Radiology*. 2002;225:300–307.

5. Foo TKF, Ho VB, Saranathan M, et al. Feasibility of integrating high-spatial-resolution 3D breath-hold coronary MR angiography with myocardial perfusion and viability examinations. *Radiology*. 2005;235:1025–1030.

6. Wang Y, Vidan E, Bergman GW. Cardiac motion of coronary arteries: variability in the rest period and implications for coronary MR angiography. *Radiology*. 1999;213:751–758.

7. Wang YI, Watts R, Mitchell IR, et al. Coronary MR angiography: selection of acquisition window of minimal cardiac motion with electrocardiography-triggered navigator cardiac motion prescanning —initial results. *Radiology*. 2001;218:580–585.

8. Danias PG, McConnell MV, Khasgiwala VC, Chuang ML, Edelman RR, Manning WJ. Prospective navigator correction of image position for coronary MR angiography. *Radiology*. 1997;203:733–736.

9. Stuber M, Botnar RM, Danias PG, Kissinger KV, Manning WJ. Submillimeter three-dimensional coronary MR angiography with real-time navigator correction: comparison of navigator locations. *Radiology*. 1999;212:579–587.

10. Coppo S, Piccini D, Bonanno G, et al. Free-running 4D whole-heart self-navigated golden angle MRI: initial results. *Magn Reson Med*. 2015;74:1306–1316.

11. Pang J, Sharif B, Fan Z, et al. ECG and navigator-free four-dimensional whole-heart coronary MRA for simultaneous visualization of cardiac anatomy and function. *Magn Reson Med*. 2014;72:1208–1217.

12. Wang Y, Rossman PJ, Grimm RC, Riederer SJ, Ehman RL. Navigator-echo-based real-time respiratory gating and triggering for reduction of respiration effects in three-dimensional coronary MR angiography. *Radiology*. 1996;198:55–60.

13. Ehman RL, McNamara MT, Pallack M, Hricak H, Higgins CB. Magnetic resonance imaging with respiratory gating: techniques and advantages. *AJR Am J Roentgenol*. 1984;143:1175–1182.

14. Piccini D, Littmann A, Nielles-Vallespin S, Zenge MO. Respiratory self-navigation for whole-heart bright-blood coronary MRI: methods for robust isolation and automatic segmentation of the blood pool. *Magn Reson Med*. 2012;68:571–579.

15. Wu HH, Gurney PT, Hu BS, Nishimura DG, McConnell MV. Free-breathing multiphase whole-heart coronary MR angiography using image-based navigators and three-dimensional cones imaging. *Magn Reson Med*. 2013;69:1083–1093.

16. Cruz G, Atkinson D, Henningsson M, Botnar RM, Prieto C. Highly efficient nonrigid motion-corrected 3D whole-heart coronary vessel wall imaging. *Magn Reson Med*. 2017;77:1894–1908.

17. Aitken AP, Henningsson M, Botnar RM, Schaeffter T, Prieto C. 100% efficient three-dimensional coronary MR angiography with two-dimensional beat-to-beat translational and bin-to-bin affine motion correction. *Magn Reson Med*. 2015;74:756–764.

18. Feng L, Axel L, Chandarana H, Block KT, Sodickson DK, Otazo R. XD-GRASP: golden-angle radial MRI with reconstruction of extra motion-state dimensions using compressed sensing. *Magn Reson Med*. 2016;75:775–788.

19. Piccini D, Feng LI, Bonanno G, et al. Four-dimensional respiratory motion-resolved whole heart coronary MR angiography. *Magn Reson Med*. 2017;77:1473–1484.

20. Feng LI, Coppo S, Piccini D, et al. 5D whole-heart sparse MRI. *Magn Reson Med*. 2018;79:826–838.

21. Fischer SE, Wickline SA, Lorenz CH. Novel real-time R-wave detection algorithm based on the vectorcardiogram for accurate gated magnetic resonance acquisitions. *Magn Reson Med*. 1999;42:361–370.

22. Larson AC, White RD, Laub G, McVeigh ER, Li D, Simonetti OP. Self-gated cardiac cine MRI. *Magn Reson Med*. 2004;51:93–102.

23. Yerly J, Ginami G, Nordio G, et al. Coronary endothelial function assessment using self-gated cardiac cine MRI and k-t sparse SENSE. *Magn Reson Med*. 2016;76:1443–1454.

24. Piccini D, Littmann A, Nielles-Vallespin S, Zenge MO. Spiral phyllotaxis: the natural way to construct a 3D radial trajectory in MRI. *Magn Reson Med*. 2011;66:1049–1056.

25. Lustig M, Donoho D, Pauly JM. Sparse MRI: the application of compressed sensing for rapid MR imaging. *Magn Reson Med*. 2007;58:1182–1195.

26. Peters DC, Derbyshire JA, McVeigh ER. Centering the projection reconstruction trajectory: reducing gradient delay errors. *Magn Reson Med*. 2003;50:1–6.

27. Grimm R, Block KT, Kiefer B, Hornegger J. Bias correction for respiration detection in radial 3D gradient-echo imaging. In: Proceedings of the 19th Annual Meeting of ISMRM, Montréal, Canada, 2011. p 2677.

28. Etienne A, Botnar RM, Van Muiswinkel AM, Boesiger P, Manning WJ, Stuber M. "Soap-Bubble" visualization and quantitative analysis of 3D coronary magnetic resonance angiograms. *Magn Reson Med*. 2002;48:658–666.

29. Moussavi A, Untenberger M, Uecker M, Frahm J. Correction of gradient-induced phase errors in radial MRI. *Magn Reson Med*. 2014;71:308–312.

30. Deshmane A, Blaimer M, Breuer F, et al. Self-calibrated trajectory estimation and signal correction method for robust radial imaging using GRAPPA operator gridding. *Magn Reson Med*. 2016;75:883–896.

31. Kramer M, Biermann J, Reichenbach JR. Intrinsic correction of system delays for radial magnetic resonance imaging. *Magn Reson Imaging*. 2015;33:491–496.

32. Chitiboi T, Feng L, Ramb R, Otazo R, Axel L. Reconstruction of arrhythmic cardiac cycles in patients with atrial fibrillation. In: Proceedings of the Joint Annual Meeting of ISMRM-ESMRMB, Paris, France, 2018. p 247.

33. Nehrke K, Bornert P, Manke D, Bock JC. Free-breathing cardiac MR imaging: study of implications of respiratory motion—initial results. *Radiology*. 2001;220:810–815.

34. Pang J, Bhat H, Sharif B, et al. Whole-heart coronary MRA with 100% respiratory gating efficiency: self-navigated three-dimensional retrospective image-based motion correction (TRIM). *Magn Reson Med*. 2014;71:67–74.

35. Han F, Rapacchi S, Khan S, et al. Four-dimensional, multiphase, steady-state imaging with contrast enhancement (MUSIC) in the heart: a feasibility study in children. *Magn Reson Med*. 2015;74:1042–1049.

36. Han F, Zhou Z, Han E, et al. Self-gated 4D multiphase, steady-state imaging with contrast enhancement (MUSIC) using rotating cartesian K-space (ROCK): validation in children with congenital heart disease. *Magn Reson Med*. 2017;78:472–483.

37. Stehning C, Bornert P, Nehrke K, Eggers H, Stuber M. Free-breathing whole-heart coronary MRA with 3D radial SSFP and self-navigated image reconstruction. *Magn Reson Med*. 2005;54:476–480.

38. Piccini D, Monney P, Sierro C, et al. Respiratory self-navigated postcontrast whole-heart coronary MR angiography: initial experience in patients. *Radiology*. 2014;270:378–386.

39. Bastiaansen J, Stuber M. Flexible water excitation for fat-free MRI at 3T using lipid insensitive binomial off-resonant RF excitation (LIBRE) pulses. *Magn Reson Med*. 2018;79:3007–3017.

40. Henglin M, Stein G, Hushcha PV, Snoek J, Wiltschko AB, Cheng S. Machine learning approaches in cardiovascular imaging. *Circ Cardiovasc Imaging*. 2017;10.

41. Slomka PJ, Dey D, Sitek A, Motwani M, Berman DS, Germano G. Cardiac imaging: working towards fully-automated machine analysis & interpretation. *Expert Rev Med Devic*. 2017;14:197–212.

SUPPORTING INFORMATION

Additional supporting information may be found online in the Supporting Information section at the end of the article.

FIGURE S1 The automatic procedure for the subject-dependent estimation of respiratory and cardiac frequency ranges from the frequency spectrum of SG signals (black line). The red bracket shows the initial frequency range of 0.5-2 Hz considered for the selection of the cardiac components from which the center of mass ($F_{0,c}$) of the spectrum is calculated. The lower bound of the frequency range ($F_{inf,c}$) is subsequently refined by finding the minimum of the spectrum within the initial interval from 0.5 Hz to $F_{0,c}$. Similarly, the upper bound of the frequency range ($F_{sup,r}$) is refined by finding the minimum within the interval from $F_{0,c}$ to 2 Hz. The procedure is then repeated for the automatic selection of the respiratory frequency range ($F_{0,r}$, $F_{inf,r}$, and $F_{sup,r}$), with 0.1-0.7 Hz as the initial interval

VIDEO S1 Transverse, coronal, and sagittal cross sections of a 5D data set reconstructed using CS and the ECG signal for cardiac binning. The top row shows cardiac motion for a fixed respiratory position at end-expiration, and the middle row shows respiratory motion for a selected bin along the cardiac motion dimension. That same bin used in combination with the end-expiratory bin leads to the motion-resolved static 3D volume in the bottom row. In this image reconstructed with ECG-gating, the selected cardiac bin corresponds to a systolic phase of the cardiac cycle

VIDEO S2 Transverse, coronal, and sagittal cross sections of a 5D data set reconstructed using CS and the SG cardiac signal for cardiac binning. The top row shows cardiac motion for a fixed respiratory position at end-expiration, and the middle row shows respiratory motion for a selected bin along the cardiac motion dimension. This bin corresponds to the same exact bin number as that used for generating the middle and bottom row displayed in Supporting Information Video S1. In combination with the end-expiratory bin, a motion-resolved static 3D volume is displayed in the bottom row. In this fully SG reconstructed image, the selected cardiac bin corresponds to a diastolic phase of the cardiac cycle